ACS APPLIED MATERIALS & INTERFACES

Research Article

www.acsami.org

4-Terminal Tandem Photovoltaic Cell Using Two Layers of PTB7:$PC_{71}BM$ for Optimal Light Absorption

Paola Mantilla-Perez,*[,†] Alberto Martinez-Otero,[†] Pablo Romero-Gomez,[†] and Jordi Martorell*[,†,§]

[†]ICFO, The Institute of Photonic Sciences Mediterranean Technology Park Castelldefels (Barcelona) 08860, Spain

[§]Departament de Física i Enginyeria Nuclear, Universitat Politècnica de Catalunya, Terrasa 08222, Spain

Supporting Information

ABSTRACT: A 4-terminal architecture is proposed in which two thin active layers (<100 nm) of PTB7:$PC_{71}BM$ are deposited on a two-sided ITO covered glass substrate. By modeling the electric field distribution inside the multilayer structure and applying an inverse solving problem procedure, we designed an optimal device architecture tailored to extract the highest photocurrent possible. By adopting such a 4-terminal configuration, we numerically demonstrated that even when the two subcells use identical absorber materials, the performance of the 4-terminal device may overcome the performance of the best equivalent single-junction device. In an experimental implementation of such a 4-terminal device, we demonstrate the viability of the approach and find a very good match with the trend of the numerical predictions.

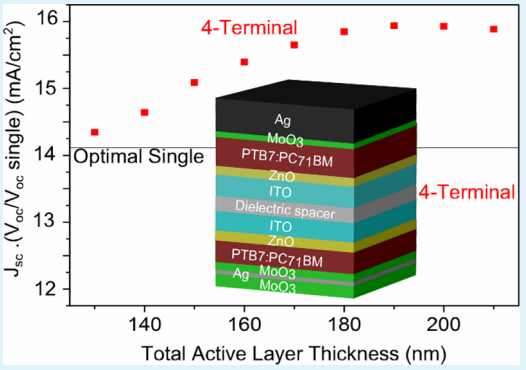

KEYWORDS: *photovoltaics, organics, dielectric spacer, 4-terminal device, optical simulations*

1. INTRODUCTION

Recent progress in the performance of solution-processed organic solar cells has consolidated them as one of the alternatives to the standard photovoltaic (PV) technology.[1] In organic PV materials, a large light absorption coefficient is combined with the mechanical flexibility of plastic materials.[2] This opens up the possibility to solar cell fabrication at room temperature with low-cost deposition techniques compatible with the use of flexible substrates. Another very interesting feature of the organic layer in a PV cell is its partial colorless transparency to visible light.[3] Flexibility and colorless transparency are key features for an optimal building integrated PV that only the organic technology may be able to offer.

In recent years, the power conversion efficiency (PCE) of single-junction organic solar cells has been rising steadily by the implementation of several strategies that, among others, include an optical optimization,[4] plasmonic enhancement,[5−8] nanostructuring of active layers,[9] new polymers design,[10−13] or interfacial engineering.[14,15] With the PTB7:$PC_{71}BM$, the average efficiency from many different research groups' best cells is 7.98%,[16] while a certified efficiency above 9% has been reported once.[14] However, further increasing the PCE is severely limited by the low charge carrier mobility.[17] Many different factors including molecular packing, disorder or low crystallinity, presence of impurities, temperature, electric field, charge-carrier density, size/molecular weight, and pressure can degrade such mobility.[18] The detrimental effects become more apparent for thicker blends by causing a dramatic reduction in fill factor (FF) for the majority of polymers.[19] Recent work explains that for sufficiently thick cells, space charge becomes more important because it creates field free regions with low collection efficiency. Doping is suggested as the dominant factor on the space charge and the thickness dependence of the performance.[20] Thus, increasing light absorption by means of thicker blends is not a viable alternative to obtain higher efficiencies. An interesting approach to increase solar cell efficiency is the tandem configuration obtained by stacking different materials with complementary absorption to harvest energy from a larger portion of the solar spectra.[21,22] In a few occasions it has been shown that with the use of tandem or triple junction devices, one may overcome the efficiency of the optimal single junction device,[23,24] setting the PCE for organic tandem cells at above 10%.[24]

Tandem solar cells design and fabrication is, however, a demanding task due to the requirement of a suitable interconnection layer (ICL) for charge recombination. The ICL must guarantee a low resistance connection that introduces no electrical potential loss, but it also has to be robust to protect the underlying layers from damage when subsequent solution processing steps to fabricate the second cell are applied.[25,26] Furthermore, the interlayer must be transparent to avoid optical losses. Additionally, the difficulty in testing the two or more cells independently makes the optimization of tandem cells a challenging task.

Herein, we report the design and fabrication of an optically optimized 4-terminal device in which two single junction

Received: May 25, 2015
Accepted: August 6, 2015
Published: August 6, 2015

DOI: 10.1021/acsami.5b04537
ACS Appl. Mater. Interfaces 2015, 7, 18435−18440

subcells are fabricated using the same blend and are separated by a SiO_2 dielectric spacer. With this architecture, we eliminate the need of an ICL and replace it by an external connection that guarantees a proper recombination. Applying an inverse solving problem procedure, we numerically designed a device architecture to obtain an optimal PV performance. In such a 4-terminal configuration, even when the two subcells use identical absorber materials, one may improve the light harvesting capacity of the best single device. In an experimental implementation of the 4-terminal device using the same polymer blend for both subcells, we find a very good match with the trend of the numerical predictions.

2. MATERIALS AND METHODS

We fabricated a 4-terminal cell by depositing each inverted subcell on either side of a bicoated ITO glass substrate. In this configuration, the dielectric spacer is a 1.1 mm thick piece of glass where a patterned ITO was deposited on one side and a second nonpatterned ITO was deposited by RF sputtering on the other side to obtain a bicoated ITO substrate. The bicoated ITO substrates were solvent cleaned and treated with ultraviolet-ozone for 10 min on each side. Fabrication of the bicoated cells was successfully carried out without damaging any of the two sides using a lightweight aluminum holder specially designed for the bifacial spin coating processes. The lightweight holder prevented any scratches on the deposited films by holding the samples only from the edges during spin coating. Additionally, to further protect the top and bottom surfaces, vertical sample holders instead of Petri dishes were used during the transportation of the substrates through the different processing steps.

The precursor for the sol–gel ZnO was prepared by dissolving zinc acetate dehydrate ($Zn(CH_3COO)_2{\cdot}2H_2O$, Aldrich, 99.9%, 1 g) and ethanolamine ($NH_2CH_2CH_2OH$, Aldrich, 99.5%, 0.28 g) in 2-methoxyethanol ($CH_3OCH_2CH_2OH$, Aldrich, 99.8%, 10 mL) under stirring for at least 12 h.[27] Afterward, it was spin-coated on the ITO and annealed at 150 °C for 10 min. The process was repeated for the other side of the ITO substrate, obtaining 30 nm thickness films. The samples were then transferred into a glovebox for further fabrication steps. An active layer of PTB7:$PC_{71}BM$, at a concentration of 10 mg/mL (1:1.5) dissolved in chlorobenzene, was spin-coated on one side of the ITO bicoated substrate. Then, 3% v/v dioodoctane (DIO) was added to the blend solution at least 1 h before spin coating. The active layer of 90 nm was left to dry in vacuum for 1 h, followed by the evaporation of MoO_3 and a thick Ag electrode. After removing the samples out of the evaporation chamber, a second active layer of 90 nm was spin-coated on the other side of the substrate and left to dry in vacuum for 1 h. A 3 nm MoO_3 layer was deposited prior to the evaporation of a thin Ag layer at a 6 Å s^{-1} rate using a homemade holder cooled down to −5 °C. To finish the structure, another layer of MoO_3 was deposited on top of the device at a rate of 1 Å s^{-1}. The last three layers formed the MoO_3/Ag (10 nm)/MoO_3 (MAM) electrode with a four point probe measured sheet resistance of 7 ohms/square. The subcells were then removed from the inert atmosphere to be externally connected in series and characterized in air.

PCE of the fabricated devices was determined from current density–voltage curve measurements obtained under 1 sun AM 1.5G spectrum from a solar simulator (Abet Technologies, model Sun 3000). A calibrated monocrystal silicon reference cell from Rera Systems was used to monitor the solar simulator intensity. EQEs were measured using a QEX10 Quantum Efficiency Measurement System from PV Measurements.

3. OPTICAL OPTIMIZATION

We consider a cell structure as the one shown in Figure 1 consisting of two single junction solar cells separated with an intermediate dielectric spacer. The structure, corresponding to a 4-terminal device in a tandem configuration, is formed by two almost identical subcells on either side of a SiO_2 dielectric

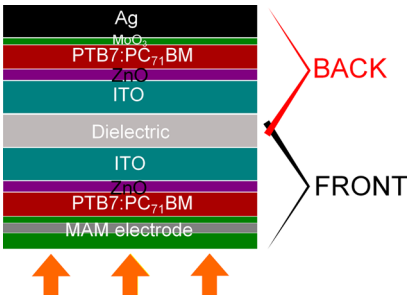

Figure 1. Device architecture.

spacer. As indicated in the previous section, up to the Ag electrode, the two subcells can be fabricated using the same processing steps, and the same blend of PTB7:$PC_{71}BM$ is used as photoactive material. The two subcells constructed in an inverted configuration use the same buffer layers, being the architecture of the anode the main difference among them. For the front cell, the outer electrode is formed by the three layer MAM structure, while for the back subcell the electrode is a thick layer of Ag (cf. Figure 1). Light enters the structure through the MAM electrode front subcell while the back subcell is illuminated with the light not absorbed by the front cell.

An optimal light absorption by both subcells may be reached when the architecture of the entire device is optimized to enhance absorption in both active layers. For the design of such optimal architecture we used an optical model based on the transfer matrix to numerically calculate the field distribution and absorption within each layer.[28−30] Incident light undergoes reflection, absorption and transmission at any of the layers of the device determined by the complex index and thickness of the given layer and the adjacent ones. The wavelength-dependent complex refractive index for the layers used in our numerical analysis is given in the Supporting Information. To optimize both cell architectures simultaneously, we followed an inverse integration procedure in which the EQEs from both cells, for 24 000 different combinations of layer thicknesses, were computed. The total number of combinations considered was determined by the number of different layer thicknesses considered for the active, HBL, thin silver, and dielectric spacer layers which were varied within the intervals given in Table 1. The ITO, MoO_3, thick silver electrode thicknesses, and the total thickness of active material were kept fixed. From the 24 000 solutions obtained, the optimal one corresponds to the one exhibiting the largest short circuit current when the currents from both cells are matched within a 0.5 mA/cm^2. To avoid any detrimental effect over the FF when real devices were to be fabricated, we restricted the thickness of either of the two blend layers to a maximum of 130 nm.

In our calculations, we considered a total active layer thickness ranging from 130 to 210 nm. The largest J_{sc} was obtained when the total blend thickness was 190 nm, distributed in a front subcell blend of 88 nm, 90 and 91 nm, together with a back subcell blend of 102 nm, 100 and 99 nm, and an Ag thickness of 10 nm, 6 and 4 nm, respectively. The dielectric spacer and ZnO thicknesses are also different, depending on the thickness of the front silver electrode. The layer thicknesses for the optimal 4-terminal device are listed in Table 1.

The optimal J_{sc} in terms of the total active layer thickness for three different configurations of the MAM electrodes and a configuration with ITO instead of MAM is shown in Figure 2a.

DOI: 10.1021/acsami.5b04537
ACS Appl. Mater. Interfaces 2015, 7, 18435−18440

Table 1. Layer Thicknesses Ranges Used in Numerical Calculations and Layer Thicknesses for the Optimal and Fabricated 4-Terminal Device

layer	range (nm)	optimal device (nm)	experimental values (nm)
total active layer (TAL)	130−210	190	180
MoO_3	fixed	39	39
Ag	4−6−10	4	10
MoO_3	fixed	3	3
PTB7:PC_{71}BM top (AL1)	70−100	91	90
ZnO	fixed	5	30
ITO	fixed	100	135
D. spacer	50−290	182	1100 μm
ITO	fixed	130	140
ZnO	5−30	8.75	30
PTB7:PC_{71}BM bottom (AL2)	TAL−AL1	99	90
MoO_3	fixed	3	3
Ag	fixed	100	100
Total Active Layer (TAL)	130−210	190	180

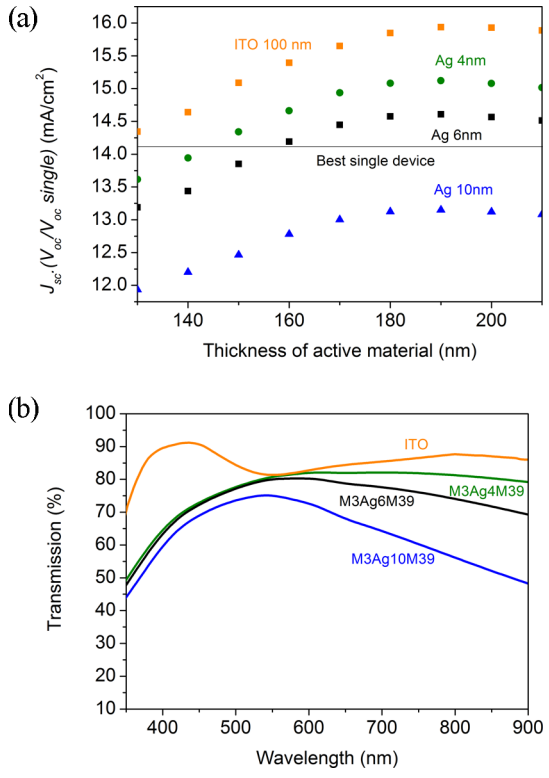

Figure 2. (a) Calculated power density normalized against the V_{oc} of a single device in terms of the total thickness of active material for the 4-terminal devices when the Ag thickness in the MAM electrode is 10 nm (blue ▲), 6 nm (black ■), 4 nm (green ●) and ITO of 100 nm (orange ■). The case of the best single device is shown in a straight line. In the graph, the power density normalized to the single device V_{oc} is used to be able to compare it with the two series connected cells which would exhibit a V_{oc} equivalent to the sum of the V_{oc} from two single junction cells. (b) Modeled spectral transmission of MAM electrodes depending on the silver thickness and ITO.

As seen in Figure 2a, the J_{sc} for the 4-terminal devices is strongly dependent on the front electrode, exhibiting a very good performance when the silver layer in the MAM is thinned down to 4 nm. This performance could be further improved if an electrode with higher transparency such as ITO were to be used. A comparison of the transmissions for the different MAM electrodes and the ITO is shown in Figure 2b. Note that the 4 or 6 nm thick Ag and ITO front electrodes of the 4-terminal devices exhibit a significantly improved performance relative to the best equivalent single junction. For the optimal 4 nm Ag MAM device, the calculated improvement relative to the best single junction reaches 7.1% and for the ITO device the improvement is almost doubled to 13%. Remarkably, such enhanced performance is obtained using the same blend in both subcells and, in a device configuration where the thickness for such layers is less than 100 nm.

The numerically calculated external quantum efficiencies (EQEs) for both subcells are shown in Figure 3a for the optimal configuration when the thickness of the Ag layer in the MAM electrode is 4 nm. At long wavelengths above 650 nm light absorption is larger in the back subcell, while at the opposite edge, for short wavelengths below 500 nm, light absorption is dominated by the front subcell. In the entire wavelength range, a local maximum in the EQE for the front subcell corresponds to a local minimum for the EQE in the back subcell and vice versa. This kind of behavior is weakly dependent on the transparency of the light entrance electrode. In Figure 3b, we show the EQEs for the optimal configuration when the thickness of the Ag electrode is 10 nm. Again, we observe that the EQE at long wavelengths is larger for the back

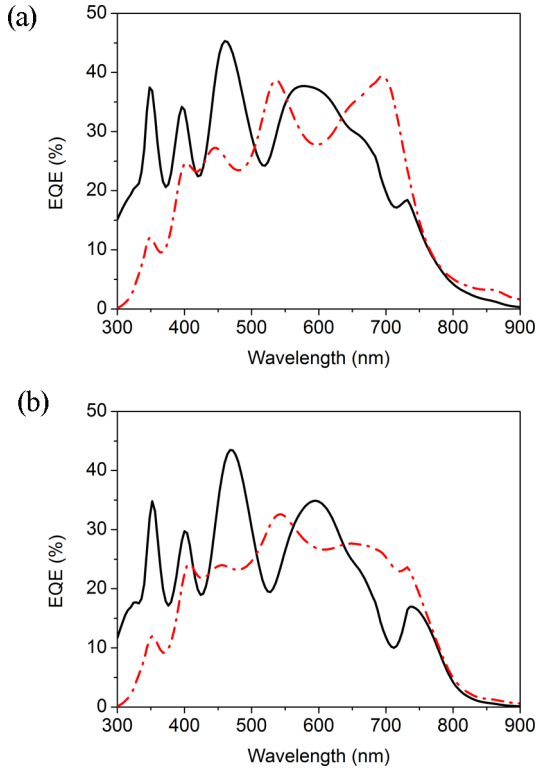

Figure 3. Numerically calculated EQE for front subcell (black continuous line) and for the back subcell (dash-dotted line) for (a) a MoO_3 (39)/Ag (4)/MoO_3 (3)/PTB7:PC_{71}BM (91)/ZnO (5)/ITO (100)/dielectric spacer (182)/ITO (130)/ZnO (8.75)/PTB7:PC_{71}BM (99)MoO_3 (3)/Ag (100) nm architecture and (b) for a MoO_3 (39)/Ag (10)/MoO_3 (3)/PTB7:PC_{71}BM (91)/ZnO (5)/ITO (100)/dielectric spacer (182)/ITO (130)/ZnO (8.75)/PTB7:PC_{71}BM (99)/MoO_3(3)/Ag (100) nm architecture.

DOI: 10.1021/acsami.5b04537
ACS Appl. Mater. Interfaces 2015, 7, 18435−18440

subcell while at shorter wavelengths is larger for the front subcell. As can be seen in Figure S2 of the SI, the observed trend in the EQE wavelength distribution between the two subcells is maintained when the thickness of the spacer layer is increased.

4. RESULTS AND DISCUSSION

The optical optimization of the multilayer structure disguises the spectral dependence to the active blend extinction coefficient leading to an EQE which is strongly linked to the electric field distribution inside the solar cell. The normalized field intensity distribution map is shown in Figure 4a as a function of wavelength and position inside the solar cell for the optimal configuration. To enhance photon harvesting, the electric field intensity must be maximized within the active layers inside the structure. As seen in Figure 4a, this electrical field intensity is clearly enhanced within the back subcell active layer for most of the wavelength range. Because of material dispersion, this confinement of the largest field density within the active layer is not so apparent for the front subcell. However, when the cell architecture is optimal, as in Figure 4a, the minima in field intensity for the front cell are, to a certain degree, compensated with field intensity maxima in the back subcell. For comparison, in Figure 4b, the field intensity distribution map is shown for a nonoptimized configuration with the same total thickness of active material. Note that in this case the field intensity in the active layer of the front subcell is weaker for almost the entire wavelength range being very apparent that the thickness of the active layer is thinner than it should be. This decrease in electric field intensity translates into a reduced photocurrent for such front subcell, thus limiting the total short-circuit current when a serial connected device is considered.

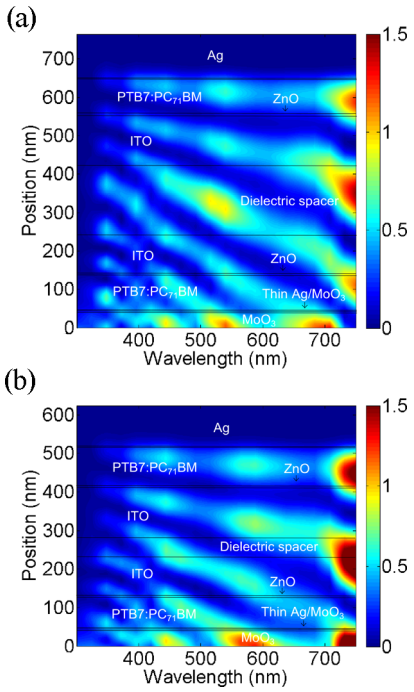

Figure 4. Calculated electric field intensity normalized with respect to the incident field intensity as a function of wavelength (a) for an optimized architecture with the following thicknesses in nm (a) a MoO_3(39)/Ag (4)/MoO_3 (3)/PTB7:PC_{71}BM (91)/ZnO (5)/ITO (100)/dielectric spacer (182)/ITO (130)/ZnO (8.75)/PTB7:PC_{71}BM (99)/MoO_3(3)/Ag (100) and (b) nonoptimized architecture with the following thicknesses in nm MoO_3(39)/Ag (4)/ MoO_3 (3)/PTB7:PC_{71}BM (80)/ZnO(5)/ITO (100)/dielectric spacer (50)/ITO (130)/ZnO (5)/PTB7:PC_{71}BM (110)/MoO_3(3)/Ag (100). The nonoptimized architecture leads to a current mismatch, originated from the bottom subcell, which generates a photocurrent above 1 mA/cm^2 with respect to the front subcell. The limiting current for this architecture remains below that of the optimized device.

One advantage of the 4-terminal tandem configuration we study over the standard 2-terminal tandem is that the performance of the two subcells can be studied independently from each other when already integrated in the entire device. An average of the PV parameters from 7 devices of 0.06 cm^2 is given in Table 2. In terms of photocurrent generation, both subcells in the implemented architecture exhibited a rather good match, which is important when the cells are connected externally in a series configuration. The match of the voltages we obtained is also desirable when the cells are connected in parallel. On the other hand, we observe that the FF for the front cell is slightly worse than the one for the back cell which may be attributed to the lower conductivity of the electrodes for the front cell when compared to the back thick silver electrode.

The $J-V$ characteristic curves for the front and back cells measured independently and externally connected in series are shown in Figure 5. We performed a statistical study to determine the average values for the J_{sc}, V_{oc}, and FF of the series connected devices. As expected the J_{sc} is limited to the smallest one of the two subcells, the V_{oc} is very close to 2 times the average V_{oc} for the single junction subcells and the FF is slightly larger than the average FF for the single junction subcells. In other words, no degradation in the electrical performance is observed for the 4-terminal device when connected in series relative to the single junction devices.

The absorbing layers were fabricated following the same recipe to obtain thicknesses of around 90 nm for both subcells, which corresponds to the thicknesses predicted by the numerical modeling of the optimal configuration. The layer architecture of the entire fabricated device is given in Table 1. At present, several experimental limitations prevent the fabrication of the optimal device according to the results

Table 2. Solar Cell Parameters

cell	J_{sc} (mA/cm)	V_{oc} (V)	FF (%)	PCE (%)
front	6.36 ± 0.28	0.703 ± 0.007	62.42 ± 2.46	2.79 ± 0.13
back	6.13 ± 0.57	0.732 ± 0.010	72.44 ± 3.07	3.25 ± 0.43
4T series	6.13 ± 0.53	1.439 ± 0.007	69.19 ± 3.14	6.10 ± 0.42
ratio of 4T in series to single subcells		0.9979[a]	1.0392[b]	

[a]The average of the sum of the front and back subcells V_{oc} in the 4-terminal devices is compared to the average of the measured V_{oc} for the serial connected cells. [b]The average FF of the independent subcells is compared to the FF of the serial connected 4-terminal devices.

DOI: 10.1021/acsami.5b04537
ACS Appl. Mater. Interfaces 2015, 7, 18435−18440

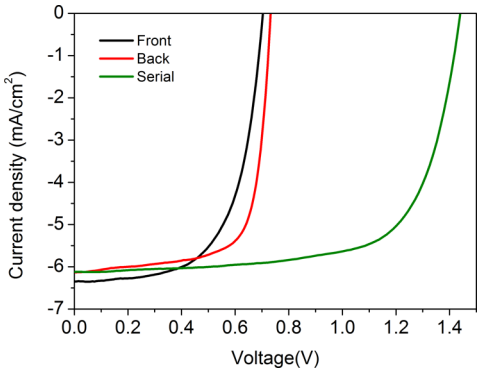

Figure 5. *I*–*V* curves of (black) front subcell, (red) back subcell, and (green) serial connected. The curves correspond to the best device.

shown in Figures 2a and 3a. Such limitations include a lack of control at the nanoscale over the thickness of the dielectric spacer; ultrathin Ag layers typically favor the formation of noncontinuous or granular films with low conductivity causing the electrical properties of the MAM electrodes to degrade rapidly when Ag thicknesses below 10 nm are considered;[31] in some cases, the optimal thickness for buffer layers extracted from the optical simulation cannot be obtained as, for instance, when the ZnO layer is prepared by sol–gel. Among these, the limited transparency of the 10 nm Ag front electrode is the largest hurdle for 4-terminal devices to overcome the performance of the single junction cell.

The experimentally measured EQEs for the front and back subcells are shown in Figure 6. Note that the interference-like

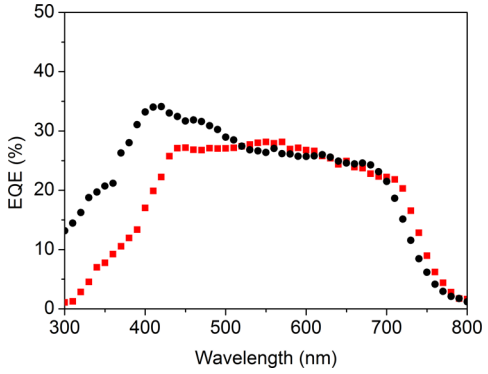

Figure 6. Measured EQE for the (black) front subcell and the (red) back subcell. Note that the large thickness of the dielectric spacer in between the two subcells eliminates the oscillatory behavior seen in the numerical prediction shown in Figure 3b.

pattern observed in Figure 3a,b is washed out because of the large thickness of the dielectric spacer which is around 1 mm in the fabricated devices. However, the overall trend of the numerically optimized EQEs is maintained in the experimentally implemented devices. As seen in Figure 6, for wavelengths larger than 700 nm, the EQE of the back subcell is large while for wavelengths below 500 nm the EQE of the front subcell dominates. In the region in between, the EQEs alternate.

5. CONCLUSION

By numerically determining the optimal layer configuration in a 4-terminal tandem cell of the same active blend, we demonstrated that it is possible to obtain devices that perform better than single-junction devices with an equivalent thickness of active material. In other words, the configuration we proposed is optimal to increase light absorption by using active layers with thicknesses below 100 nm, which is the limit thickness to reach good electrical performance for the majority of the low band gap polymer cells.[32] We have used the optical simulations as a guideline to fabricate a proof of principle 4-terminal device using PTB7:$PC_{71}BM$ blend as the blend material for the active layers of two inverted subcells. We fabricated the two subcells on each side of a 1.1 mm thick glass substrate coated on both sides with ITO. The overall trend of light harvesting capacity seen in the experimentally measured EQEs for the two subcells of the fabricated devices is in agreement with the EQEs predicted by the optical model. We have demonstrated that no degradation in the electrical performance of the 4-terminal cell relative to the single junction devices is seen when the two subcells are connected in a series configuration. At present, the strongest limitation to obtaining 4-terminal devices with a performance overcoming the performance of an equivalent single junction device is in the limited transparency of the front semitransparent electrode. Provided that semitransparent electrodes that can be deposited on top of polymer cells, such as electrodes composed of Ag nanowires[33] or graphene,[34] were to be used, the 4-terminal device performance would be considerably improved and most certainly surpass the one from the single-junction device. We demonstrated this numerically by considering an ITO front electrode. Finally, one should note that the 4-terminal device has some advantages over the traditional tandem series connected approach. Cells can be connected either in series or in parallel while current or voltage matching would not strictly be necessary if the cells were made to operate independently.

■ ASSOCIATED CONTENT

Supporting Information

The Supporting Information is available free of charge on the ACS Publications website at DOI: 10.1021/acsami.5b04537.

Refractive indexes for the different materials used in the numerical simulations and EQE for subcells when the thickness of the spacer layer is increased. (PDF)

■ AUTHOR INFORMATION

Corresponding Authors

*E-mail: paola.mantilla@icfo.es.
*E-mail: jordi.martorell@icfo.es.

Notes

The authors declare no competing financial interest.

■ ACKNOWLEDGMENTS

This project has received funding from the European Union's FP7 research and innovation programme under grant agreement No. 604506 and by the Ministerio de Economia y Competitividad under grant IPT-2012- 0986-120000.

■ REFERENCES

(1) Scharber, M. C.; Sariciftci, N. S. Efficiency of Bulk-heterojunction Organic Solar Cells. *Prog. Polym. Sci.* **2013**, *38*, 1929–1940.
(2) Hadipour, A.; de Boer, B.; Wildeman, J.; Kooistra, F. B.; Hummelen, J. C.; Turbiez, M. G. R.; Wienk, M. M.; Janssen, R. a. J.; Blom, P. W. M. Solution-Processed Organic Tandem Solar Cells. *Adv. Funct. Mater.* **2006**, *16*, 1897–1903.

DOI: 10.1021/acsami.5b04537
ACS Appl. Mater. Interfaces 2015, 7, 18435–18440

(3) Betancur, R.; Romero-Gomez, P.; Martinez-Otero, A.; Elias, X.; Maymó, M.; Martorell, J. Transparent Polymer Solar Cells Employing a Layered Light-trapping Architecture. *Nat. Photonics* **2013**, *7*, 995−1000.
(4) Martinez-Otero, A.; Elias, X.; Betancur, R.; Martorell, J. High-Performance Polymer Solar Cells Using an Optically Enhanced Architecture. *Adv. Opt. Mater.* **2013**, *1*, 37−42.
(5) Li, X.; Choy, W. C. H.; Lu, H.; Sha, W. E. I.; Ho, A. H. P. Efficiency Enhancement of Organic Solar Cells by Using Shape-Dependent Broadband Plasmonic Absorption in Metallic Nanoparticles. *Adv. Funct. Mater.* **2013**, *23*, 2728−2735.
(6) Zarick, H. F.; Hurd, O.; Webb; Joseph, A.; Hungerford, C.; Erwin; William, R.; Bardhan, R. Enhanced Efficiency in Dye-Sensitized Solar Cells with Shape-Controlled Plasmonic Nanostructures. *ACS Photonics* **2014**, *1*, 806−811.
(7) Pastorelli, F.; Bidault, S.; Martorell, J.; Bonod, N. Self-Assembled Plasmonic Oligomers for Organic Photovoltaics. *Adv. Opt. Mater.* **2014**, *2*, 171−175.
(8) In, S.; Mason, D. R.; Lee, H.; Jung, M.; Lee, C.; Park, N. Enhanced Light Trapping and Power Conversion Efficiency in Ultrathin Plasmonic Organic Solar Cells: A Coupled Optical-Electrical Multiphysics Study on the Effect of Nanoparticle Geometry. *ACS Photonics* **2015**, *2* (1), 78−85.
(9) Babu, V. J.; Vempati, S.; Sundarrajan, S.; Sireesha, M.; Ramakrishna, S. Effective Nanostructured Morphologies for Efficient Hybrid Solar Cells. *Sol. Energy* **2014**, *106*, 1−22.
(10) Dou, L.; Gao, J.; Richard, E.; You, J.; Chen, C.-C.; Cha, K. C.; He, Y.; Li, G.; Yang, Y. Systematic Investigation of Benzodithiophene- and Diketopyrrolopyrrole-based Low-bandgap Polymers Designed for Single Junction and Tandem Polymer Solar Cells. *J. Am. Chem. Soc.* **2012**, *134*, 10071−10079.
(11) Dou, L.; Chang, W.-H.; Gao, J.; Chen, C.-C.; You, J.; Yang, Y. A Selenium-Substituted Low-bandgap Polymer with Versatile Photovoltaic Applications. *Adv. Mater.* **2013**, *25*, 825−831.
(12) Li, W.; Hendriks, K. H.; Roelofs, W. S. C.; Kim, Y.; Wienk, M. M.; Janssen, R. a J. Efficient Small Bandgap Polymer Solar Cells with High Fill Factors for 300 nm Thick Films. *Adv. Mater.* **2013**, *25*, 3182−3186.
(13) Guo, X.; Zhou, N.; Lou, S. J.; Smith, J.; Tice, D. B.; Hennek, J. W.; Ortiz, R. P.; Navarrete, J. T. L.; Li, S.; Strzalka, J.; Chen, L. X.; Chang, R. P. H.; Facchetti, A.; Marks, T. Polymer Solar Cells with Enhanced Fill Factors. *Nat. Photonics* **2013**, *7*, 825−833.
(14) He, Z.; Zhong, C.; Su, S.; Xu, M.; Wu, H.; Cao, Y. Enhanced Power-conversion Efficiency in Polymer Solar Cells Using an Inverted Device Structure. *Nat. Photonics* **2012**, *6*, 591−595.
(15) Woo, S.; Hyun Kim, W.; Kim, H.; Yi, Y.; Lyu, H.-K.; Kim, Y. 8.9% Single-Stack Inverted Polymer Solar Cells with Electron-Rich Polymer Nanolayer-Modified Inorganic Electron-Collecting Buffer Layers. *Adv. Energy Mater.* **2014**, *4*, 1301692.
(16) Lu, L.; Yu, L. Understanding Low Bandgap Polymer PTB7 and Optimizing Polymer Solar Cells Based on It. *Adv. Mater.* **2014**, *26*, 4413−4430.
(17) Janssen, R. a J.; Nelson, J. Factors Limiting Device Efficiency in Organic Photovoltaics. *Adv. Mater.* **2013**, *25*, 1847−1858.
(18) Coropceanu, V.; Cornil, J.; da Silva, D.; Olivier, Y.; Silbey, R.; Brédas, J. L. Charge Transport in Organic Semiconductors. *Chem. Rev.* **2007**, *107*, 926−952.
(19) Peet, J.; Wen, L.; Byrne, P.; Rodman, S.; Forberich, K.; Shao, Y.; Drolet, N.; Gaudiana, R.; Dennler, G.; Waller, D. Bulk Heterojunction Solar Cells with Thick Active Layers and High Fill Factors Enabled by a Bithiophene-co-thiazolothiazole Push-pull Copolymer. *Appl. Phys. Lett.* **2011**, *98*, 043301.
(20) Kirchartz, T.; Agostinelli, T.; Campoy-Quiles, M.; Gong, W.; Nelson, J. Understanding the Thickness-Dependent Performance of Organic Bulk Heterojunction Solar Cells: The Influence of Mobility, Lifetime, and Space Charge. *J. Phys. Chem. Lett.* **2012**, *3*, 3470−3475.
(21) Ameri, T.; Dennler, G.; Lungenschmied, C.; Brabec, C. J. Organic Tandem Solar Cells: A Review. *Energy Environ. Sci.* **2009**, *2*, 347−363.
(22) Andersson, B. V.; Wuerfel, U.; Inganäs, O. Full Day Modelling of V-shaped Organic Solar Cell. *Sol. Energy* **2011**, *85*, 1257−1263.
(23) Li, W.; Furlan, A.; Hendriks, K. H.; Wienk, M. M.; Janssen, R. a J. Efficient Tandem and Triple-junction Polymer Solar Cells. *J. Am. Chem. Soc.* **2013**, *135*, 5529−5532.
(24) You, J.; Dou, L.; Yoshimura, K.; Kato, T.; Ohya, K.; Moriarty, T.; Emery, K.; Chen, C.-C.; Gao, J.; Li, G.; Yang, Y. A Polymer Tandem Solar Cell with 10.6% Power Conversion Efficiency. *Nat. Commun.* **2013**, *4*, 1446.
(25) Yang, J.; Zhu, R.; Hong, Z.; He, Y.; Kumar, A.; Li, Y.; Yang, Y. A Robust Inter-connecting Layer for Achieving High Performance Tandem Polymer Solar Cells. *Adv. Mater.* **2011**, *23*, 3465−3470.
(26) Li, N.; Baran, D.; Forberich, K.; Turbiez, M.; Ameri, T.; Krebs, F. C.; Brabec, C. J. An Efficient Solution-Processed Intermediate Layer for Facilitating Fabrication of Organic Multi-Junction Solar Cells. *Adv. Energy Mater.* **2013**, *3*, 1597−1605.
(27) Sun, Y.; Seo, J.; Takacs, C. J.; Seifter, J.; Heeger, A. J. Inverted Polymer Solar Cells Integrated with a Low-temperature-annealed Sol-gel-derived ZnO Film as an Electron Transport Layer. *Adv. Mater.* **2011**, *23*, 1679−1683.
(28) Betancur, R.; Martinez-Otero, A.; Elias, X.; Romero-Gomez, P.; Colodrero, S.; Miguez, H.; Martorell, J. Optical Interference for the Matching of the External and Internal Quantum Efficiencies in Organic Photovoltaic Cells. *Sol. Energy Mater. Sol. Cells* **2012**, *104*, 87−91.
(29) Pettersson, L. A. A.; Roman, L. S.; Inganäs, O. Modeling Photocurrent Action Spectra of Photovoltaic Devices Based on Organic Thin Films. *J. Appl. Phys.* **1999**, *86*, 487−496.
(30) Yeh, P. *Optical Waves in Layered Media*, 2nd ed; Wiley: New York, 1988.
(31) Sergeant, N. P.; Hadipour, A.; Niesen, B.; Cheyns, D.; Heremans, P.; Peumans, P.; Rand, B. P. Design of Transparent Anodes for Resonant Cavity Enhanced Light Harvesting in Organic Solar Cells. *Adv. Mater.* **2012**, *24*, 728−732.
(32) Martinez-Otero, A.; Liu, Q.; Mantilla-Perez, P.; Montes Bajo, M.; Martorell, J. An Extremely Thin and Robust Interconnecting Layer Providing 76% Fill Factor in a Tandem Polymer Solar Cell Architecture. *J. Mater. Chem. A* **2015**, *3*, 10681−10686.
(33) Guo, F.; Kubis, P.; Stubhan, T.; Li, N.; Baran, D.; Przybilla, T.; Spiecker, E.; Forberich, K.; Brabec, C. J. Fully Solution-Processing Route Toward Highly Transparent Polymer Solar Cells. *ACS Appl. Mater. Interfaces* **2014**, *6* (20), 18251−18257.
(34) He, M.; Jung, J.; Qiu, F.; Lin, Z. Graphene-based Transparent Flexible Electrodes for Polymer Solar Cells. *J. Mater. Chem.* **2012**, *22*, 24254.

DOI: 10.1021/acsami.5b04537
ACS Appl. Mater. Interfaces 2015, 7, 18435−18440